Pixelated non-volatile programmable photonic integrated circuits with 20-level intermediate states

Wenyu Chen[1], Shiyuan Liu[1,2,*] and **Jinlong Zhu[1,2,*]**

[1] State Key Laboratory of Intelligent Manufacturing Equipment and Technology, Huazhong University of Science and Technology, Wuhan 430074, People's Republic of China
[2] Optics Valley Laboratory, Wuhan, Hubei 430074, People's Republic of China

E-mail: shyliu@hust.edu.cn and jinlongzhu03@hust.edu.cn

Abstract

Multi-level programmable photonic integrated circuits (PICs) and optical metasurfaces have gained widespread attention in many fields, such as neuromorphic photonics, optical communications, and quantum information. In this paper, we propose pixelated programmable Si_3N_4 PICs with record-high 20-level intermediate states at 785 nm wavelength. Such flexibility in phase or amplitude modulation is achieved by a programmable Sb_2S_3 matrix, the footprint of whose elements can be as small as 1.2 μm, limited only by the optical diffraction limit of an in-house developed pulsed laser writing system. We believe our work lays the foundation for laser-writing ultra-high-level (20 levels and even more) programmable photonic systems and metasurfaces based on phase change materials, which could catalyze diverse applications such as programmable neuromorphic photonics, biosensing, optical computing, photonic quantum computing, and reconfigurable metasurfaces.

Supplementary material for this article is available online

Keywords: programmable photonic integrated circuits, phase change materials, multi-level intermediate states, metasurfaces

1. Introduction

Photonic integrated circuits (PICs), particularly those based on silicon photonics, have emerged as powerful platforms in a variety of fields, such as optical communications [1], sensors [2, 3], photonic neural networks [4–7], and quantum computing [8]. Programmable photonic devices, as one of the key components in PICs, perform linear and non-linear optical operations through optical manipulation technologies

[9–12]. In silicon photonic platforms, the thermo-optical effect and plasma dispersion effect are commonly used to change the refraction index of silicon for optical phase shifts. However, these phase modulation approaches offer only small changes in the refractive index and require large photonic device footprints [13]. Moreover, microheater-induced thermal crosstalk and free-carrier-induced optical absorption impede the development of large-scale PICs.

Due to the large refractive index contrast ($\Delta n > 1$) between the amorphous and crystalline states of chalcogenide phase change materials (PCMs), PCMs have been used as a kind of reconfigurable material in rewritable compact discs [14]. Recently, researchers have investigated PCMs in nanophotonic platforms to perform programmable optical functions, including optical memories [15, 16], reconfigurable metasurfaces [17, 18], photonic switches [19], and

---

neuromorphic photonics [20, 21]. Compared to traditional optical modulators, a significant advantage of PCMs is that they can maintain the phase state without additional energy, i.e. non-volatile. In addition, PCMs have prominent advantages such as large refractive index contrasts between different states, rapid and reversible switching between amorphous and crystalline states, excellent stability at room temperature, and high reproducibility (up to 10^{12}) [22]. Germanium-antimony-telluride (GST) is the most widely used PCM in nanophotonics due to its high refractive index contrast and outstanding stability [23]. However, the phase transition of GST from the amorphous to the crystalline state causes an increase in both the real and imaginary parts of the refractive index. Crystalline GST with a high extinction coefficient results in a heavy absorption of light in the visible and near-infrared regimes, which makes GST a suitable material for performing optical intensity modulation in intensity-coded photonic systems [24, 25]. However, low-loss optical phase modulators are required for programmable photonic circuits, particularly Mach–Zehnder interferometer (MZI)-based architectures. Moreover, the optical loss induced by GST destroys the unitary properties of MZI meshes [26, 27]. Recently, wide-bandgap PCMs, such as GSST, Sb_2S_3, and Sb_2Se_3, have been investigated to reduce the optical loss in photonic interferometers and micro-ring resonators [28–36]. While there has been significant research development on low-loss PCMs in the amorphous and crystalline states, the study of the multilevel intermediate states at the micron scale is still in its infancy [37]. The research on programmable PCM-based PICs and metasurfaces primarily utilized thermal annealing and electrothermal switching [38–41]. As a result, programmable PICs and metasurfaces with ultra-high flexibility in phase modulation using multi-level PCMs with free-space laser switching were rarely reported, to the best of our knowledge.

In this paper, we propose a pixelated programmable Si_3N_4 photonic circuit with record-high 20-level intermediate states at 785 nm wavelength. Such a high degree of freedom in phase or amplitude modulation is achieved by a programmable Sb_2S_3 matrix, the footprint of whose elements can be as small as 1.2 μm, limited only by the optical diffraction limit. Moreover, we demonstrated the partial crystalline induced by the multiple laser pulse strategy is more stable and has a finer phase transition than the single-pulse strategy by using an in-house developed multi-level pulsed laser writing system alongside a portfolio of optical nanometrology technologies (see more details in the supplementary materials). We have shown the potential for improving the number of intermediate states of a single Sb_2S_3 element by precisely optimizing the power and number of pulses. By utilizing multilevel intermediate states achieved by our in-house developed micron-scale laser writing system, we simulated an Sb_2S_3-based phase shifter in a programmable MZI and demonstrated that it could achieve 30-level phase shift accuracy of π at 785 nm wavelength. In addition, we simulated the programmable 1×2 switch by precisely adjusting the level of crystallization of the Sb_2S_3 pixels on a multimode interferometer (MMI). In this way, we have demonstrated the availability

of very large-scale pixelated non-volatile programmable PICs by simulation. We believe this work lays the foundation for laser-writing multi-level PICs and metasurfaces based on low-loss PCMs, and, therefore, opens up its potential applications in neuromorphic photonics, optical computing, photonic quantum computing, and reconfigurable metasurfaces.

2. Pixelated non-volatile programmable PICs

The proposed pixelated non-volatile programmable PICs are shown in figure 1. The architecture of the programmable photonic circuits consists of cascaded MZIs to perform matrix–vector multiplication (MVM), which is the main mathematical operation in artificial neural networks [4]. The unitary transformation matrix $U(n)$ can be decomposed into the product of multiple unitary matrix $U(2)$, and each unitary matrix $U(2)$ is achieved by the basic programmable MZI unit. Each programmable MZI unit contains two 50:50 beam splitters and two Sb_2S_3-based pixelated phase shifters (outer phase shifter ϕ and inner phase shifter θ). The basic unitary matrix $U(2)$ of each MZI unit is given by

$$U(2) = je^{j(\theta/2)} \begin{pmatrix} e^{j\phi} \sin\frac{\theta}{2} & \cos\frac{\theta}{2} \\ e^{j\phi} \cos\frac{\theta}{2} & -\sin\frac{\theta}{2} \end{pmatrix} \quad (1)$$

The low-loss Sb_2S_3 materials are deposited on the waveguides to act as phase shifters. By precisely controlling the power and number of the laser pulses, the focused laser beam is used to realize multi-level intermediate states of Sb_2S_3 pixels with a length of 1 μm. The multi-level intermediate states of Sb_2S_3 pixels with different refractive indices can realize multi-level phase shifts with almost no energy loss. The movable laser writing system (with more details regarding figure 3 and the supplementary material) is used to switch multiple Sb_2S_3 pixels, as shown in figure 1. By combining multi-level intermediate states with micron-scale laser writing, 30-level/π phase shift accuracy can be achieved, which meets the requirements of artificial neural networks. In addition, compared to GST materials with large absorption loss, low-loss Sb_2S_3-based phase shifters have the potential to be applied in very large-scale PICs (up to 100×100).

3. Results and discussion

3.1. Optical characterization of Sb_2S_3 material

In order to apply Sb_2S_3 in the field of pixelated programmable PICs, it is essential to determine the refractive index (real part n and imaginary part k) of amorphous Sb_2S_3 (aSbS) and crystalline Sb_2S_3 (cSbS) and the crystallization temperature. A 10 nm-thick Sb_2S_3 film was deposited by radio frequency (RF) sputtering on a standard 500 μm-thick silicon substrate. After that, a 20 nm-thick SiO_2 film, which acts as the protective layer, was deposited by PECVD at 100 °C to prevent sulfur loss during the phase transition process. The schematic diagram of the multi-layer sample is shown in figure 2(a). The
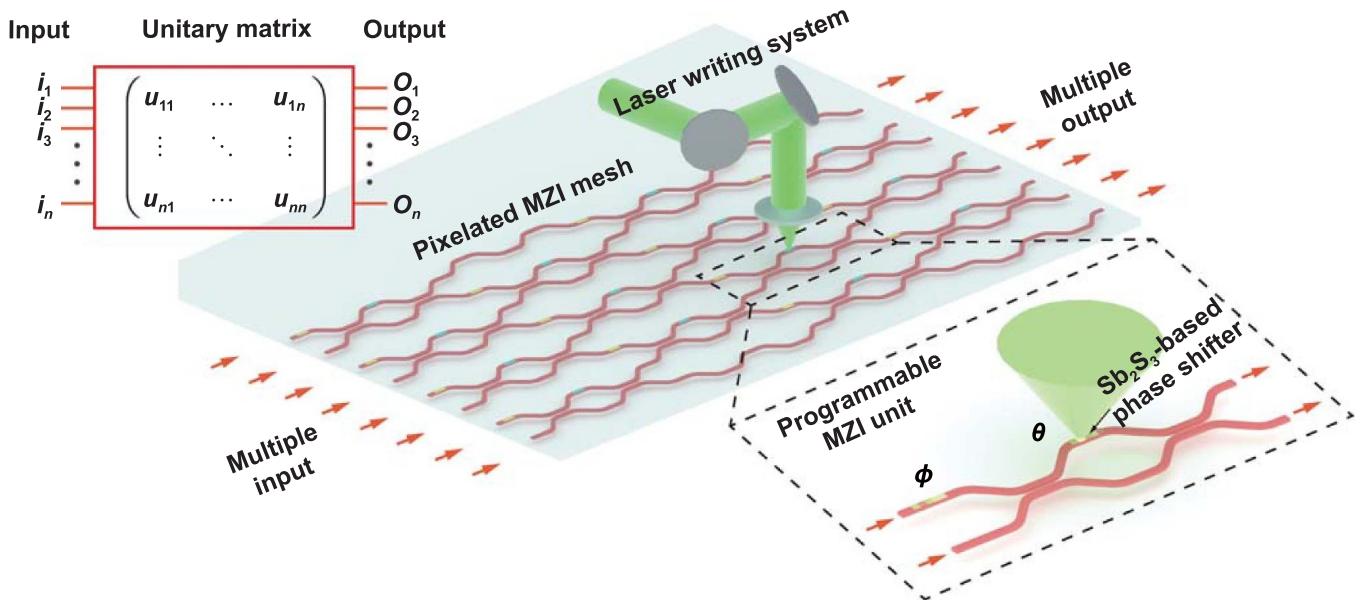
Figure 1. Pixelated programmable non-volatile photonic integrated circuits. The pixelated MZI mesh performs unitary transformation from input to output.
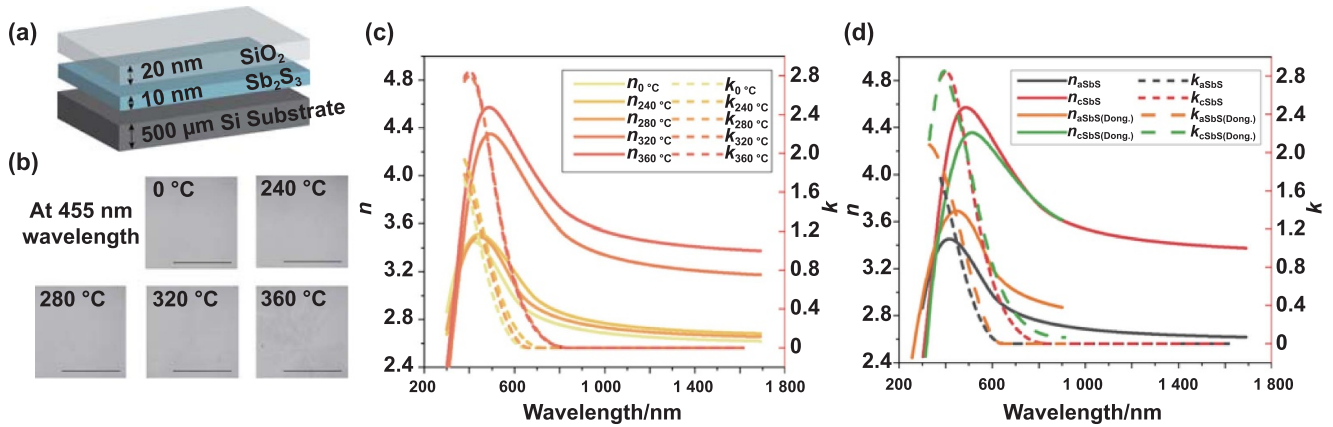

Figure 2. Optical characterization of Sb_2S_3 material. (a) The schematic diagram of the Sb_2S_3 sample. (b) Optical microscope images of the Sb_2S_3 samples heated at different temperatures. The scale bar is 50 μm. (c) The refractive indexes of five Sb_2S_3 samples heated at different temperatures, which were measured by a spectroscopic ellipsometer. (d) The reconstructed optical constants are compared with those in [35].

deposited Sb_2S_3 material at the very beginning was in the amorphous state. To crystallize the Sb_2S_3 film and determine the crystallization temperature, four Sb_2S_3 samples were annealed at different temperatures (starting from 240 °C to 360 °C with an increment of 40 °C) for 5 min. As shown in figure 2(b), the film surface shows a non-uniform pattern when the heating temperature reaches up to 320 °C, which is due to the nucleation and growth of crystals. The optical constants of the originally deposited Sb_2S_3 sample and four Sb_2S_3 samples heated at different temperatures are measured by a spectroscopic ellipsometer, as illustrated in figure 2(c). More details on the ellipsometer can be found in the supplementary material. As expected from the Sb_2S_3 micrographs, the Sb_2S_3 starts to crystallize at 320 °C, after which the refractive index changes dramatically. According to the measurement results, the fitted bandgaps of cSbS and aSbS are 1.53 eV and

2.04 eV, respectively. The bandgaps of amorphous and crystalline Sb_2S_3 are much larger than those of GST, which means that Sb_2S_3 could significantly reduce optical loss compared to GST in the visible and near-IR wavebands [36]. As shown in figure 2(d), the refractive indexes of aSbS and cSbS were compared with other measurement results from [35]. The slight difference may be caused by the material roughness, the fabrication process, or the measurement error.

3.2. Laser-writing multi-level intermediate states of Sb_2S_3 elements

A programmable multi-level Sb_2S_3 matrix consists of a large number of Sb_2S_3 elements. The fine phase transition and the footprint of a single Sb_2S_3 element are crucial for the performance of the programmable PICs and metasurfaces. In this
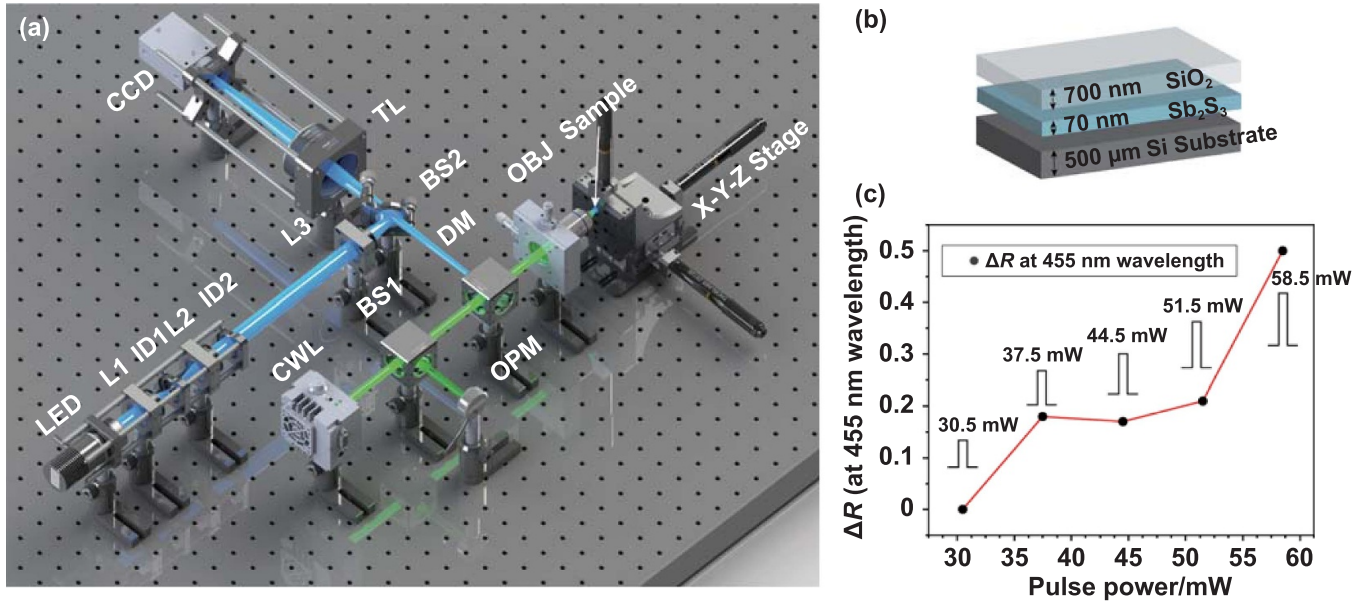
Figure 3. The pulsed laser writing system and the measured reflectance that reflects the multi-level intermediate states of Sb_2S_3 elements. (a) The experimental setup of the pulsed laser writing system. L, lens; ID, iris diaphragm; CWL: continuous wave lasers; BS, beam splitter; OPM, optical power meter; DM, dichroic mirror; OBJ, objective lens; TL, tube lens. (b) The schematic diagram of the Sb_2S_3 sample. (c) The measured reflectance that reflects the different intermediate states of Sb_2S_3 elements at different laser powers (from 30.5 mW to 58.5 mW).

section, we investigate the laser-writing multi-level intermediate states of a single Sb_2S_3 element at the microscale. A 70 nm-thick Sb_2S_3 film was deposited on the silicon substrate, after which a 700 nm-thick SiO_2 was deposited as the protective layer. The experimental setup of the in-house developed pulsed laser writing system for the multi-level phase transition of Sb_2S_3 matrix can be found in figures 3(a) and S1: a high-power laser beam generated by a continuous wave laser (CWL) at 520 nm wavelength is focused by a 50×/0.6NA objective lens on single Sb_2S_3 elements to perform phase transition. The full width at half maximum (FWHM) of the focused laser spot size is 1.2 μm. According to the transfer matrix method, the degree of crystallization of Sb_2S_3 elements can be characterized by the reflectance of the phase-change region [42, 43]. An optical brightfield microscope was then added to the laser-writing setup in order to navigate the region of interest and measure the reflectance of phase-transition regions *in-situ*. The illumination and imaging light paths are shown in blue in figure 3(a). The central wavelength and the bandwidth (FWHM) of the LED are 455 nm and 18 nm, respectively. The power of the LED is too low to impact the phase transition. More details about the experimental setup can be found in supplementary materials.

Single laser pulses with different powers were used to induce different degrees of crystallization of Sb_2S_3 elements. The laser power generated by the laser diode changes from 30.5 mW to 58.5 mW, and the laser pulse duration is 10 ms. The reflectance difference (ΔR) is used to determine the crystallize fraction given by

$$\Delta R = \frac{R - Ra}{Ra} \qquad (2)$$

where R is the measured reflectance of intermediate states of Sb_2S_3 elements, and R_a is the reflectance of aSbS. The ΔR of the phase-change regions at different laser powers was measured and shown in figure 3(c). When the laser power is too low (less than 30.5 mW) to reach the crystallization temperature, there is no change in the reflectance of the Sb_2S_3, and the Sb_2S_3 pixel remains in the amorphous state. As the laser power increases from 37.5 mW to 51.5 mW with a step of 7 mW, the aSbS starts to partially crystallize and the reflectance increases before reaching up to the peak reflectance (i.e. the point where full crystallization happens). A slight variation in the reflectance of intermediate states of Sb_2S_3 can be observed when the laser power is increased from 37.5 mW to 51.5 mW. The underlying physics of why ΔR remains the same at pulse power ranging from 37.5 mW to 51.5 mW, unfortunately, is unknown as of now, but it again demonstrates the fact that the relationship between laser power and the reflectance difference is nonlinear [44]. Hence, we would like to leave this as an open question for future study and discussion, while focusing on the demonstration of the multi-level intermediate states of Sb_2S_3 alongside its potential applications in this paper. As we increase the pulse power from 51.5 mW to 58.5 mW, we observe a further increase in the reflectance difference, which indicates the generation of more intermediate states. In addition, the central damage of phase-change regions affects the stability of crystallization [32, 36]. Due to the low absorption of aSbS and the burn-in-effect, local damage and defects can be induced by the high-power and long-period laser pulse illumination in the phase-change regions. The central damage images of Sb_2S_3 elements after high laser power excitation are shown in figure S2. As a result, the crystallization stability of Sb_2S_3 induced by a single high-power and long-duration
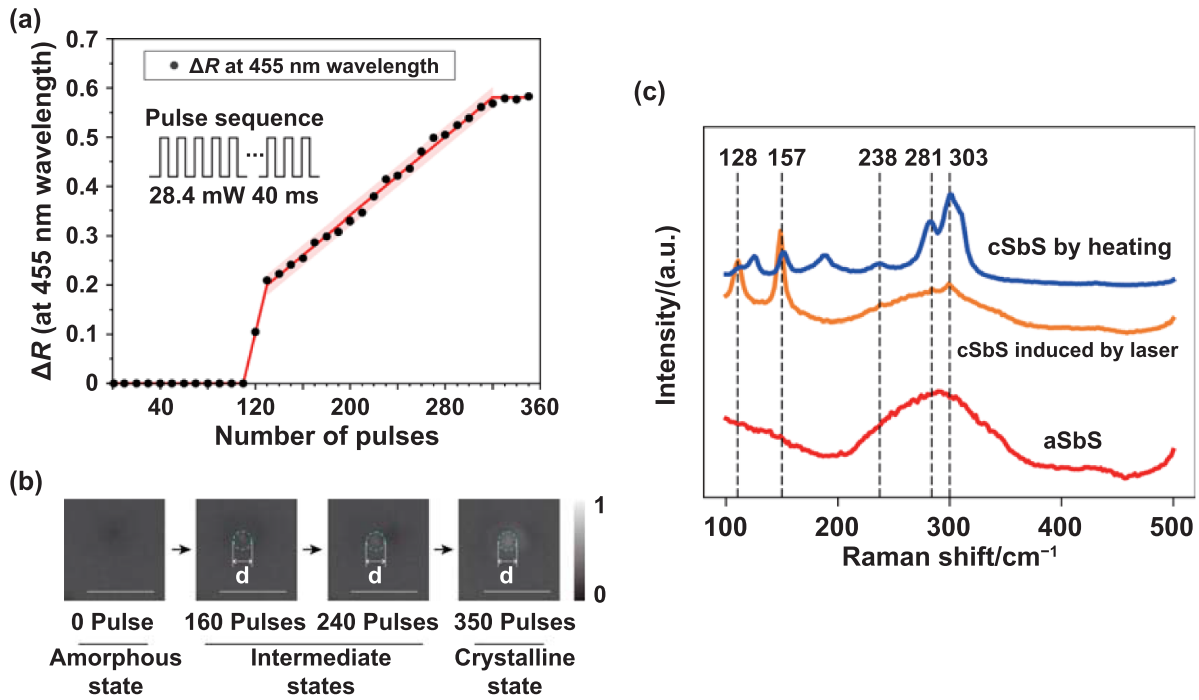
Figure 4. Multi-level intermediate states of Sb_2S_3 induced by different numbers of laser pulses. (a) The ΔR of intermediate states of Sb_2S_3 elements induced by different numbers of laser pulses (from 0 to 350 pulses). (b) The optical microscope images of the phase-transition pixels under different numbers of pulses (0, 160, 240, 350). The Sb_2S_3 pixel without laser pulse illumination is in the amorphous state; the aSbS pixels after the illumination by the number of pulses in 160 and 240 are in the intermediate states; the aSbS elements excited by 350 pulses are in the fully crystalline state. The scale bar is 5 μm. (c) Raman spectra of aSbS and cSbS induced by thermal annealing and the focused laser.

laser pulse limits the applications of multi-level intermediate states.

To improve the crystallization stability, we use different numbers of low-power laser pulses to crystallize aSbS pixels (from 0 to 350 pulses). The power of the laser beam is 28.4 mW, and the pulse period and duty cycle of the square pulses are 80 ms and 50%, respectively. The reflectance of the Sb_2S_3 induced by different numbers of pulses was measured, as shown in figure 4(a). The microscopic images of the phase-transition pixel under different numbers of pulses (0, 160, 240, 350) are shown in figure 4(b). The microscopic images of 20-level intermediate states are illustrated in figure S3. When the number of pulses is less than 120, the reflectance remains constant because the temperature of the laser heating area does not reach the crystalline temperature (around 320 °C). As the number of pulses exceeds 120, the reflectance gradually increases. The increase in reflectance is linearly related to the number of pulses. The reflectance difference reaches its peak value of 0.58 after 320 laser pulses. In comparison, the reflectance difference of cSbS heated on a heating panel is 0.60, which is slightly higher than that of cSbS pixels induced by the focused laser. This indicates that the reflectance difference between Sb_2S_3 induced by thermal annealing and the focused laser demonstrates the complete crystallization after 320 laser pulses. The gradual increase in reflectance and absence of darker points in the phase-change region exclude the influence of local damage induced by high-power laser pulses. In addition, we performed the measurement of Raman spectrum to demonstrate the cSbS induced by laser pulses, as shown in figure 4(c). The Sb_2S_3 processed by thermal annealing and laser heating has the same set of peak wavelengths corresponding to known vibration modes that affirm crystallization [32]. The experimental results demonstrate the efficiency of the laser heating process in the crystallization of PCMs. The 20-level intermediate states of single Sb_2S_3 pixels were realized in the range of 120–320 pulses. The diameter of the phase-transition pixels is about 1.2 μm, which is caused by the focused laser. Compared with the single-pulse crystallization strategy, the partial crystallization strategy using low-power, multi-pulse lasers is much more stable. The longer period and pulse interval allow for a longer duration of heat transfer from the center to the edge in the phase-transition region, alleviating the issue of excessive temperature in the center of the phase-transition region. Therefore, the multiple low-power pulse crystallization approach is more suitable for achieving multi-level intermediate states. Moreover, the multi-pulse crystallization approach has also been demonstrated to greatly improve cycling durability [34]. We set 10 pulses as the crystallization step to guarantee the distinct reflectance difference of 20-level intermediate states and improve the stability of crystallization. The slope of ΔR with the number of pulses could go down with a proper reduction in optical power. The more intermediate states of Sb_2S_3 pixels could be realized by optimizing the pulse power and pulse duration.
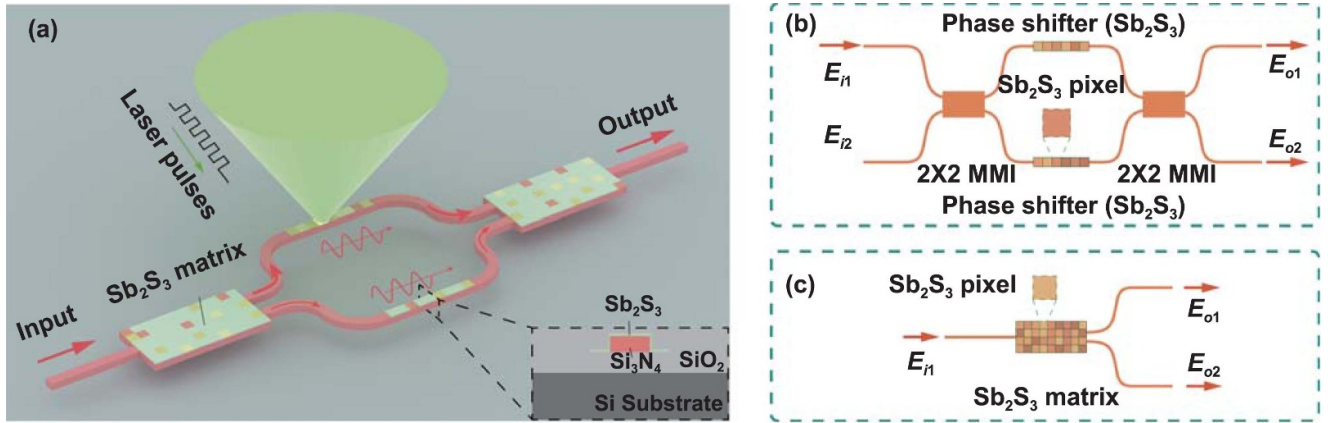
Figure 5. Pixelated non-volatile programmable photonic integrated circuits. (a) The schematic diagram of the pixelated non-volatile programmable photonic integrated circuits based on multi-level intermediate states. The inset denotes the cross-section of the waveguide. (b) The programmable MZI, in which Sb_2S_3 pixels are used to modulate the optical phase. (c) The programmable 1×2 optical switch based on Sb_2S_3 matrix.

In addition, more precise measuring instruments are required to distinguish the minor reflectance differences of different intermediate states of Sb_2S_3 pixels. While the main focus of this paper is the crystallization of Sb_2S_3, it is worth noting that multi-level intermediate states during the amorphization process can also be realized in a similar way [34, 44]. Compared to the crystallization process, the amorphization process requires higher temperature and shorter laser pulse width (from femtoseconds to nanoseconds). The parameters of laser pulses, including the laser power, the pulse width and the repetition frequency, need to be optimized through experiments to realize multi-level intermediate states. In terms of cyclability, there were some studies discussing the cycling duration of PCMs, especially Sb_2S_3 [34, 36]. Delaney *et al* [36] demonstrated a fast degradation of Sb_2S_3 after around 1000 switching cycles. To improve the cycling durability, [34] demonstrated a multi-pulse irradiation-based method to obtain greater cycling durability. It is worth noting that the region irradiated by laser pulses tends to form irreversible deformation due to local melting and surface tension, while lowering pulse energy reduces the deformation and thus improves cycling durability. Compared with a single pulse with high energy, the method of using multiple pulses with lower pulse power tends to improve the cycling durability.

3.3. Pixelated non-volatile programmable Si₃N₄ photonic circuits

The programmable integrated photonic circuits based on programmable MZIs have been proposed to perform various linear functions, such as MVM, which behaves similarly to the field programmable gate arrays in electronic integrated circuits [45]. The MZIs, as basic building blocks, consist of thermal phase shifters with a large footprint, which impede very large-scale integration of PICs. In this section, we propose pixelated non-volatile programmable PICs based on multi-level intermediate states of Sb_2S_3 pixels, as shown in

figure 5(a). The low-loss Sb_2S_3 is first deposited on the multimode interferometer (MMI) and waveguide, after which a movable laser spot is focused on the different Sb_2S_3 pixels to induce partial crystallization. The Sb_2S_3 pixels are then switched to intermediate states to affect light propagation. In this paper, we simulated two fundamental pixelated programmable photonic integrated devices, i.e. programmable MZI and MMI, to demonstrate the feasibility of the programmable Sb_2S_3 matrix in PICs, as shown in figures 5(b) and (c). The multi-level intermediate states of Sb_2S_3 used in the simulation are determined by our experimentally characterized Sb_2S_3 thin film. The cross-section of the sample is shown in figure 6(a), which is consistent with the structure used in simulation. The thickness of Sb_2S_3 film is 10 nm, which was determined through simulation optimization. Additionally, a 200 nm-thick Si_3N_4 film was prepared for waveguides. Five-level intermediate states of 10 nm-thick Sb_2S_3 pixels were realized experimentally; see the micro images in figure 6(b). The diameter of phase-transition pixels is 1 μm, which corresponds to the spot size of the focused laser. Based on the reflectance of the Sb_2S_3 pixels at intermediate states, the crystalline fraction can be determined, and the effective permittivity (ε_{eff}) and the refractive index of intermediate Sb_2S_3 pixels can be calculated according to the effective medium theory [46] (see more details in the supplementary materials).

Firstly, we simulated the symmetrical MZI at 785 nm wavelength. A Sb_2S_3 film was assumed to be deposited on two arms of the MZI to modulate the optical phase without damaging the unitary properties. The width and height of the Si_3N_4 waveguide are 500 nm and 200 nm respectively, to determine the single-mode condition. Because the thickness of the Sb_2S_3 film affects the optical mode in the waveguides and therefore, the phase modulation and the optical loss, we simulated Sb_2S_3 films of different thicknesses (from 10 nm to 30 nm) on the waveguides to determine the appropriate thickness of the Sb_2S_3 layer for phase modulation. The figure of merit (FOM) $\Delta n_{eff}/\Delta k_{eff}$ was used to estimate the loss of the
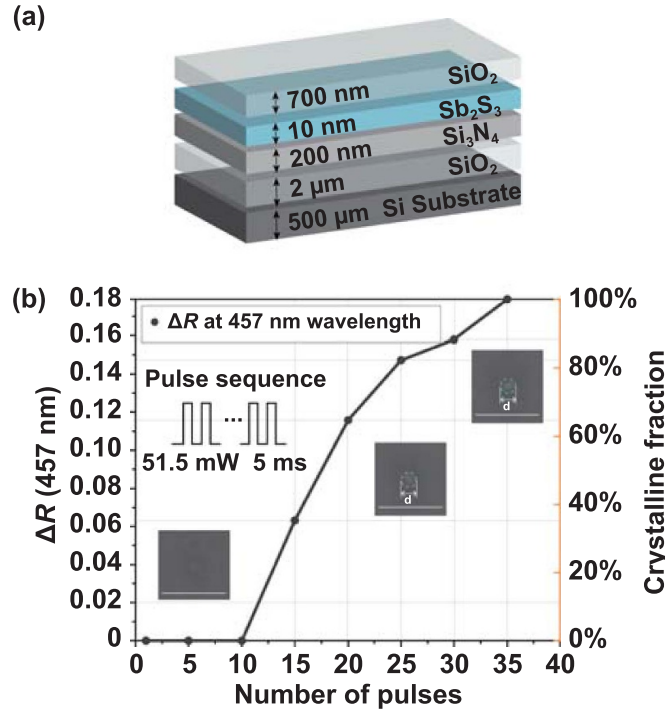
Figure 6. 5-level intermediate states of 10 nm-thick Sb_2S_3 pixels. (a) The cross-section of the 10 nm-thick Sb_2S_3 layer on the Si_3N_4 layer. (b) The ΔR of Sb_2S_3 pixels as a function of intermediate states.
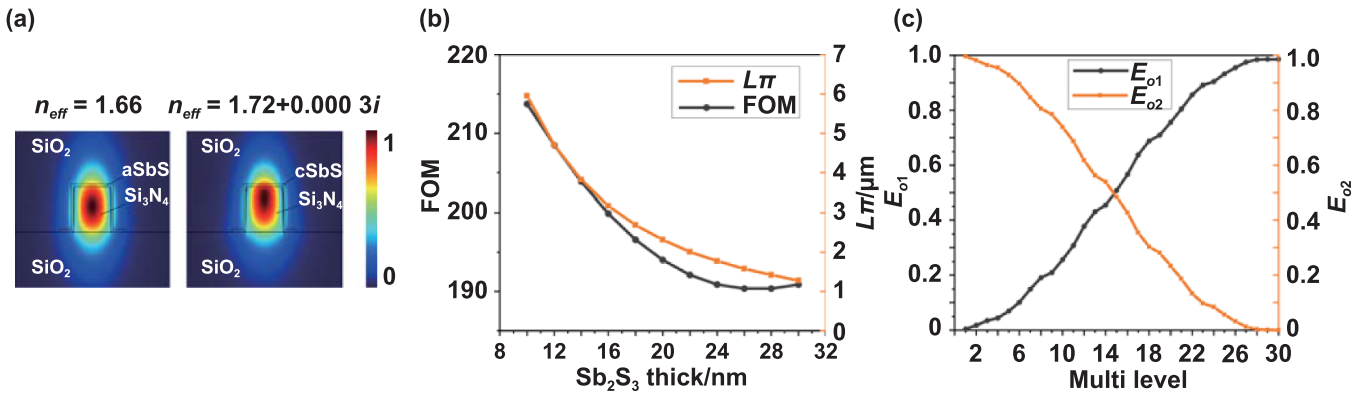

Figure 7. The programmable MZI based on multi-level intermediate states of Sb_2S_3 pixels. (a) The normalized intensity distribution of waveguide mode for aSbS (left) and cSbS (right). (b) The FOM and L_π of different thicknesses of Sb_2S_3 films. (c) The simulated transmission of bar (E_{o1}) and cross (E_{o2}) outputs of the MZI.

cSbS phase shifters, and $L\pi$ is the length of the Sb_2S_3 patch to realize the π phase shift in each waveguide arm. The simulated results are shown in figure 7(b). Apparently, a thinner Sb_2S_3 film with a larger $L\pi$ corresponds to a higher FOM. In addition, the mode overlaps between bare waveguides and waveguides covered with Sb_2S_3 are higher for thinner Sb_2S_3 films. The simulated results of mode overlaps are shown in figure S5. This means that the 10 nm-thick Sb_2S_3 film has a lower optical insertion loss. Thus, a 10 nm-thick Sb_2S_3 matrix was applied in the MZIs, and the simulation electric field intensity profile can be seen in figure 7(a). By combining the 5-level intermediate states and the number of laser-writing Sb_2S_3 pixels, we simulated the 30-level transmission of bar and cross output

(E_{o1} and E_{o2}), as shown in figure 7(c). It is worth noting that the simulated MZI can return to the initial state by inducing Sb_2S_3 pixels to the initial amorphous state [29].

In addition, we studied the programmable Si_3N_4 MMI based on the Sb_2S_3 matrix to perform a 1×2 switch at a 785 nm wavelength in simulation. As shown in figure 8, the width and length of Sb_2S_3 matrix are 4 μm and 17 μm, respectively. The size of a reconfigurable Sb_2S_3 pixel is 1×1 μm, and the thickness of Sb_2S_3 film remains the same as before (i.e. 10 nm). The total number of pixels is 68 (4×17). The Sb_2S_3 pixels are in the initial amorphous state, and the MMI performs a 50:50 power split, as shown in figures 8(a) and (b). To switch the optical power to the
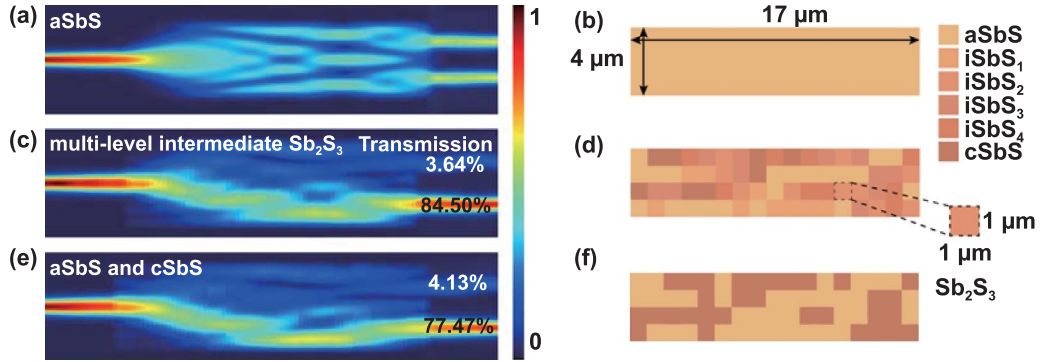
Figure 8. Optically programmable MMI based on multi-level Sb_2S_3 matrix. The normalized intensity distribution shown in (a), (c) and (e) correspond to (b) the uniform aSbS, (d) the programmed multi-level Sb_2S_3 matrix, and (f) the programmed binary Sb_2S_3 matrix, respectively. The simulation was implemented by the 3D eigenmode expansion method.

lower waveguide, we optimize the intermediate states of the Sb_2S_3 matrix in the MMI region based on a multiple-value search algorithm. Each Sb_2S_3 pixel has six intermediate states, which correspond to six refractive index values, i.e. 2.75 (aSbS), $3.042 + 0.000777i$ (iSbS$_1$), $3.355 + 0.00182i$ (iSbS$_2$), $3.561 + 0.002635i$ (iSbS$_3$), $3.643 + 0.002985i$ (iSbS$_4$), $3.819 + 0.0038i$ (cSbS), which have been experimentally determined in the previous section. Similar to the direct-binary-search algorithm, we provide a random pattern as the initial guess. The state of one Sb_2S_3 pixel is switched, and the FOM is simulated in one simulation. The state of the pixel is retained if the FOM is improved; otherwise, the pixel is brought back to its previous state. In this way, all 68 pixels with 6 values are simulated in one iteration. When the FOM stops improving after several iterations, we can ensure that the best results are obtained. As shown in figures 8(c) and (d), 84.50% transmission of the lower waveguide is obtained. For comparison, we also optimized the same Sb_2S_3 matrix size but with only two states for each pixel, i.e. aSbS and cSbS. The simulated results along with the pattern of the Sb_2S_3 matrix are shown in figures 8(d) and (f). The transmission (77.47%) of the binary Sb_2S_3 matrix configuration is apparently lower than that of the multi-level Sb_2S_3 matrix. The simulated results of the programmable MMI demonstrate the superior performance achieved with the multi-level Sb_2S_3 compared to binary Sb_2S_3. Moreover, the multi-level Sb_2S_3 induced by the focused laser pulses has more potential applications in programmable PICs and metasurfaces than the Sb_2S_3 with only binary states. As an example, we proposed and simulated a single-layer continuous varifocal metalens based on multi-level Sb_2S_3 pixels. More details of the metalens can be found in the supplementary materials.

3.4. Pixelated programmable MZI-based photonic linear processor

To validate the proposed pixelated PICs, an MZI-based photonic linear processor that uses Sb_2S_3-based pixelated phase shifters is realized by simulation, as shown in figure 9. The structure of the photonic linear processor is shown in figure 1, and the Sb_2S_3-based phase shifters with 30-level/π

accuracy are used in the photonic linear processor. The photonic linear processor is used to perform convolution between kernels and an image, as shown in figure 9(a). The photonic system with nine inputs can perform simultaneous convolution on an image with nine 3×3 kernels. Each 3×3 kernel filter is flattened into a 1×9 row vector, and the resulting nine kernel vectors form the 9×9 kernel matrix M. Then the kernel matrix M is decomposed as $M = U\Sigma V^\dagger$ based on singular value decomposition. U and $V^\dagger$ are unitary matrices, which can be decomposed into multiple cascaded MZIs using the Clements' scheme [47], and the diagonal matrix Σ is implemented by a column of MZIs. The raw image is divided into multiple 3×3 patches, and then flattened into column vectors as inputs. The input signals propagate through the Sb_2S_3-based kernel matrix to realize MVM and convolution. The nine outputs from o_1 to o_9 correspond to nine kernel filters, and the sequence of outputs is reshaped into processed images. The raw image and processed images are shown in figure 9(a). The whole pixelated kernel matrix and Sb_2S_3-based phase shift values are shown in figure S7.

To validate the accuracy of pixelated kernel matrix in very large-scale PICs, we generated random unitary matrices $U(16)$ and $U(64)$. The unitary matrices are decomposed into cascaded MZIs, and the phase shifters are discretized into multi-level phase values. The inner phase shifts θ (range from 0 to π) are discretized to 30-level phase values, and the outer phase shifters ϕ (range from $-\pi$ to π) are discretized into 60-level phase values. Then the discrete matrices ($U_P(16)$ and $U_P(64)$) and the error matrices are shown in figure 9(b). Moreover, a standard measure of fidelity is used to quantify the performance of the pixelated matrix. The fidelity is given by

$$F = \left| \frac{tr\left(U_P^\dagger U\right)}{\sqrt{N \times tr\left(U^\dagger U\right)}} \right|^2, \tag{3}$$

where N is the number of inputs. The simulated fidelity of pixelated matrices is shown in figure 9(c). The fidelity of the very large-scale MZI mesh (100×100) is maintained at above 90%. Overall, the simulation results indicate that the pixelated programmable MZI-based photonic linear processor has the potential to be scaled up to a large size.
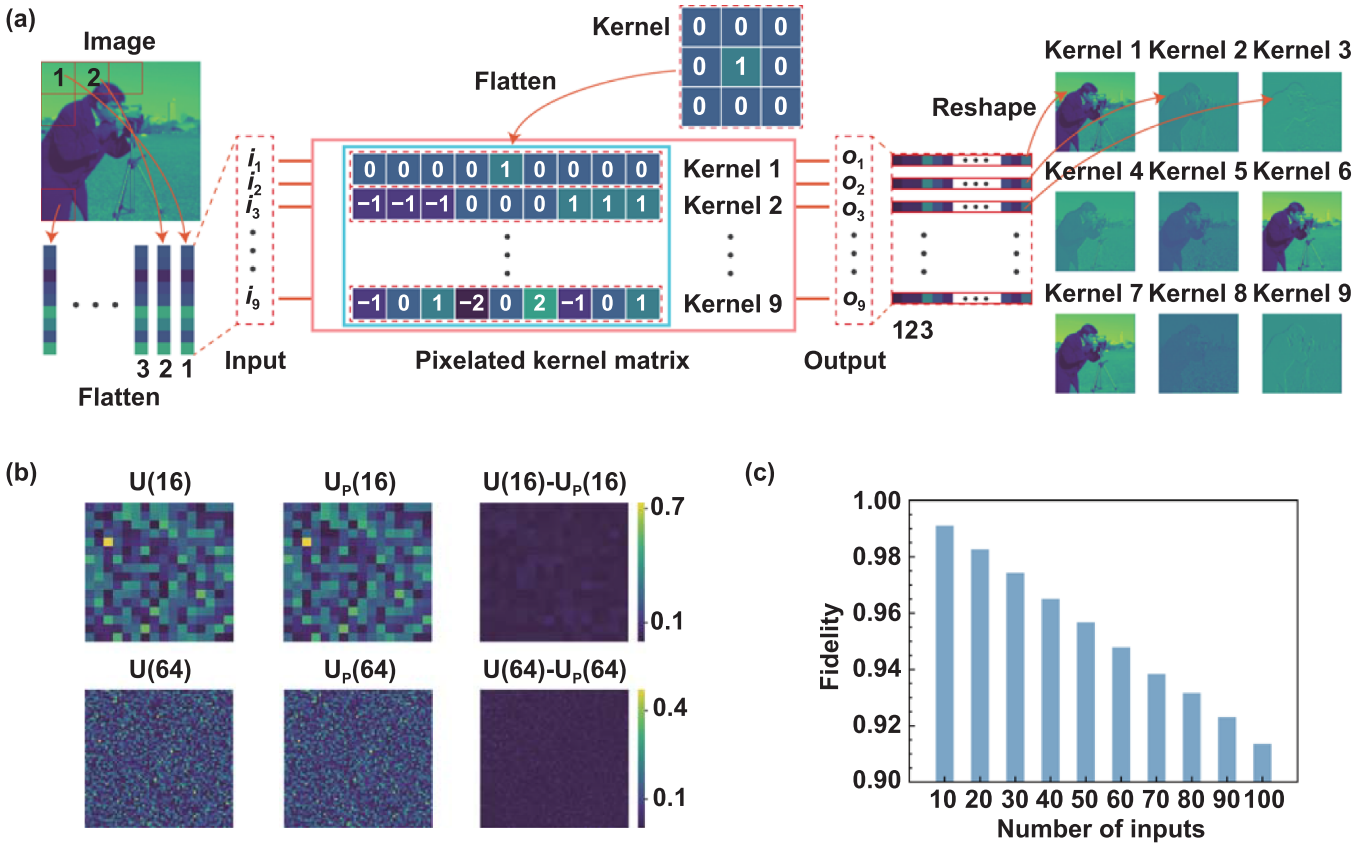
Figure 9. The pixelated programmable MZI-based photonic linear processor. (a) The schematic of the pixelated photonic linear processor. (b) The element values of the unitary matrix ($U(16)$ and $U(64)$), the recovered matrices ($U_P(16)$ and $U_P(64)$) and the error matrices ($U_d(16)$ and $U_d(64)$). (c) The fidelity of the pixelated matrix.

4. Conclusion

In this work, we proposed and demonstrated the pixelated programmable Si_3N_4 photonic circuits with record-high 20-level intermediate states at 785 nm wavelength by utilizing a programmable Sb_2S_3 matrix. The 20-level intermediate states of each programmable Sb_2S_3 element have a minimal 1.2 μm footprint, limited only by the optical diffraction limit of the in-house developed multi-pulse laser-writing system. Moreover, we have shown the potential of further improving the number of intermediate states of a single Sb_2S_3 element by precisely optimizing the power and number of pulses. We believe the Sb_2S_3-matrix-based programmable PICs could have a positive impact on general-purpose programmable photonic circuits and photonic neural networks. Moreover, we hope our work could open up the applications of laser-induced programmable devices for neuromorphic photonics, optical computing, photonic quantum computing, and reconfigurable metasurfaces.

5. Fabrication

5.1. Fabrication of Sb_2S_3 samples

Sb_2S_3 thin films were deposited on the silicon substrates (N-type, 100) under vacuum by RF magnetron sputtering using an Sb_2S_3 target. Ar gas was introduced into the chamber at a flow rate of 20 sccm, and the magnetron sputtering power was 20 W. The deposited speed was 1.37 nm·min^{-1}, which was measured by an optical ellipsometer. Then, a SiO_2 cladding layer was deposited by PECVD at 100 °C, which is lower than the crystalline temperature of Sb_2S_3.

5.2. Suggested fabrication method for pixelated PICs

The proposed pixelated PICs can be fabricated based on the existing silicon photonics fabrication technology. The suggested fabrication process can be detailed as follows.

A 200 nm-thick Si_3N_4 film is deposited on SiO_2 (2 μm) on the silicon substrates by PECVD process, after which the photonic circuits can be fabricated using three-step deep ultra-violet lithography or electron-beam lithography process. The first lithography step is prepared for fabricating alignment markers. The resist that is spin-coated on the wafer is selectively exposed for making the alignment markers. Then the resist is developed using specific solvents. The gold and chromium are evaporated over the whole wafer by electron-beam evaporation. The sacrificial layer (unexposed resist) is washed away in acetone, and the gold on the sacrificial layer is lifted off together with the sacrificial layer. Then, the gold in direct contact with the substrate remains and is formed into alignment markers. The second lithography step is used to

fabricate the Si$_3$N$_4$ waveguides. The lithography process is similar to the first lithography step. The distinct steps involve replacing the lift-off process with an etching process. The Si$_3$N$_4$ film is etched by the inductively coupled plasma etching. Then the resist is removed in acetone. The third lithography process is used to fabricate the Sb$_2$S$_3$ pixels. The fabrication process is similar to the first step. The Sb$_2$S$_3$ material is deposited by RF magnetron sputtering (in the section 5.1). Finally, the chip is cladded by the SiO$_2$ as a protective layer via low-temperature PECVD.

After fabricating PICs, the pulsed laser writing system can be used to create pixelated non-volatile programmable PICs, see more details in section 3.2. By controlling the position of the laser beam with the objective lens and the sample stage, a programmable Sb$_2$S$_3$ matrix can be achieved. The resolution of the laser writing system is only limited by the optical diffractive limit. The laser power and the number of laser pulses are controlled to induce multi-level intermediate states of the Sb$_2$S$_3$ pixels. The states and phase values of the Sb$_2$S$_3$ pixels are determined by the calibration experiments, as detailed in sections 2 and 3.

Acknowledgments

ORCID iDs

Shiyuan Liu ⓘ https://orcid.org/0000-0002-0756-1439
Jinlong Zhu ⓘ https://orcid.org/0000-0002-5723-2879

References

[1] Bogaerts W and Chrostowski L 2018 Silicon photonics circuit design: methods, tools and challenges *Laser Photon. Rev.* **12** 1700237

[2] Wang J W, Sanchez M M, Yin Y, Herzer R, Ma L B and Schmidt O G 2020 Silicon-based integrated label-free optofluidic biosensors: latest advances and roadmap *Adv. Mater. Technol.* **5** 1901138

[3] Wang J F, Suo J, Song Z X, Li W J and Wang Z B 2023 Nanomaterial-based flexible sensors for metaverse and virtual reality applications *Int. J. Extrem. Manuf.* **5** 032013

[4] Shen Y C *et al* 2017 Deep learning with coherent nanophotonic circuits *Nat. Photon.* **11** 441–6

[5] Zhou K *et al* 2023 Manufacturing of graphene based synaptic devices for optoelectronic applications *Int. J. Extrem. Manuf.* **5** 042006

[6] Ashtiani F, Geers A J and Aflatouni F 2022 An on-chip photonic deep neural network for image classification *Nature* **606** 501–6

[7] Zhu Y X, Mao H W, Zhu Y, Wang X J, Fu C Y, Ke S, Wan C J and Wan Q 2023 CMOS-compatible neuromorphic devices for neuromorphic perception and computing: a review *Int. J. Extrem. Manuf.* **5** 042010

[8] Mehta K K, Zhang C, Malinowski M, Nguyen T L, Stadler M and Home J P 2020 Integrated optical multi-ion quantum logic *Nature* **586** 533–7

[9] Mennea P L *et al* 2018 Modular linear optical circuits *Optica* **5** 1087–90

[10] Harris N C *et al* 2018 Linear programmable nanophotonic processors *Optica* **5** 1623–31

[11] Pérez D, Gasulla I and Capmany J 2018 Field-programmable photonic arrays *Opt. Express* **26** 27265–78

[12] Liao K, Li C T, Dai T X, Zhong C Y, Lin H T, Hu X Y and Gong Q H 2022 Matrix eigenvalue solver based on reconfigurable photonic neural network *Nanophotonics* **11** 4089–99

[13] Reed G T, Mashanovich G, Gardes F Y and Thomson D J 2010 Silicon optical modulators *Nat. Photon.* **4** 518–26

[14] Wuttig M, Bhaskaran H and Taubner T 2017 Phase-change materials for non-volatile photonic applications *Nat. Photon.* **11** 465–76

[15] Ríos C, Stegmaier M, Hosseini P, Wang D, Scherer T, Wright C D, Bhaskaran H and Pernice W H P 2015 Integrated all-photonic non-volatile multi-level memory *Nat. Photon.* **9** 725–32

[16] Li X, Youngblood N, Ríos C, Cheng Z G, Wright C D, Pernice W H and Bhaskaran H 2019 Fast and reliable storage using a 5 bit, nonvolatile photonic memory cell *Optica* **6** 1–6

[17] Zhang Y F *et al* 2021 Electrically reconfigurable non-volatile metasurface using low-loss optical phase-change material *Nat. Nanotechnol.* **16** 661–6

[18] Abdollahramezani S *et al* 2022 Electrically driven reprogrammable phase-change metasurface reaching 80% efficiency *Nat. Commun.* **13** 1696

[19] Xu P P, Zheng J J, Doylend J K and Majumdar A 2019 Low-loss and broadband nonvolatile phase-change directional coupler switches *ACS Photonics* **6** 553–7

[20] Cheng Z G, Ríos C, Pernice W H P, Wright C D and Bhaskaran H 2017 On-chip photonic synapse *Sci. Adv.* **3** e1700160

[21] Feldmann J, Youngblood N, Wright C D, Bhaskaran H and Pernice W H P 2019 All-optical spiking neurosynaptic networks with self-learning capabilities *Nature* **569** 208–14

[22] Abdollahramezani S, Hemmatyar O, Taghinejad H, Krasnok A, Kiarashinejad Y, Zandehshahvar M, Alù A and Adibi A 2020 Tunable nanophotonics enabled by chalcogenide phase-change materials *Nanophotonics* **9** 1189–241

[23] Zhang W, Mazzarello R, Wuttig M and Ma E 2019 Designing crystallization in phase-change materials for universal memory and neuro-inspired computing *Nat. Rev. Mater.* **4** 150–68

[24] Teo T Y, Teo T Y, Krbal M, Mistrik J, Mistrik J, Prikryl J, Lu L, Simpson R E and Simpson R E 2022 Comparison and analysis of phase change materials-based reconfigurable silicon photonic directional couplers *Opt. Mater. Express* **12** 606–21

[25] Simpson R E, Yang J K W and Hu J J 2022 Are phase change materials ideal for programmable photonics?: opinion *Opt. Mater. Express* **12** 2368–73

[26] Pai S, Bartlett B, Solgaard O and Miller D A B 2019 Matrix optimization on universal unitary photonic devices *Phys. Rev. Appl.* **11** 064044

[27] Bogaerts W, Pérez D, Capmany J, Miller D A B, Poon J, Englund D, Morichetti F and Melloni A 2020 Programmable photonic circuits *Nature* **586** 207–16

[28] Zhang Y F *et al* 2019 Broadband transparent optical phase change materials for high-performance nonvolatile photonics *Nat. Commun.* **10** 4279

[29] Liu H L, Dong W L, Wang H, Lu L, Ruan Q F, Tan Y S, Simpson R E and Yang J K W 2020 Rewritable color nanoprints in antimony trisulfide films *Sci. Adv.* **6** eabb7171

[30] Fang Z R *et al* 2022 Ultra-low-energy programmable non-volatile silicon photonics based on phase-change materials with graphene heaters *Nat. Nanotechnol.* **17** 842–8

[31] Teo T Y, Ma X X, Pastor E, Wang H, George J K, Yang J K W, Wall S, Miscuglio M, Simpson R E and Sorger V J 2022 Programmable chalcogenide-based all-optical deep neural networks *Nanophotonics* **11** 4073–88

[32] Gutiérrez Y *et al* 2022 Interlaboratory study on Sb_2S_3 interplay between structure, dielectric function, and amorphous-to-crystalline phase change for photonics *iScience* **25** 104377

[33] Fang Z R, Zheng J J, Saxena A, Whitehead J, Chen Y Y and Majumdar A 2021 Non-volatile reconfigurable integrated photonics enabled by broadband low-loss phase change material *Adv. Opt. Mater.* **9** 2002049

[34] Gao K, Du K, Tian S M, Wang H, Zhang L, Guo Y X, Luo B C, Zhang W D and Mei T 2021 Intermediate phase-change states with improved cycling durability of Sb_2S_3 by femtosecond multi-pulse laser irradiation *Adv. Funct. Mater.* **31** 2103327

[35] Dong W L, Liu H L, Behera J K, Lu L, Ng R J H, Sreekanth K V, Zhou X L, Yang J K W and Simpson R E 2019 Wide bandgap phase change material tuned visible photonics *Adv. Funct. Mater.* **29** 1806181

[36] Delaney M, Zeimpekis I, Lawson D, Hewak D W and Muskens O L 2020 A new family of ultralow loss reversible phase-change materials for photonic integrated circuits: Sb_2S_3 and Sb_2Se_3 *Adv. Funct. Mater.* **30** 2002447

[37] Delaney M, Zeimpekis I, Du H, Yan X Z, Banakar M, Thomson D J, Hewak D W and Muskens O L 2021 Nonvolatile programmable silicon photonics using an ultralow-loss Sb_2Se_3 phase change material *Sci. Adv.* **7** eabg3500

[38] Zhang H Y, Zhang H Y, Yang X, Lu L J, Chen J P, Rahman B M A and Zhou L J 2021 Comparison of the phase change process in a GST-loaded silicon waveguide and MMI *Opt. Express* **29** 3503–14

[39] Zheng J J *et al* 2020 Nonvolatile electrically reconfigurable integrated photonic switch enabled by a silicon PIN diode heater *Adv. Mater.* **32** 2001218

[40] Wei M L *et al* 2023 Electrically programmable phase-change photonic memory for optical neural networks with nanoseconds in situ training capability *Adv. Photon.* **5** 046004

[41] Meng J W *et al* 2023 Electrical programmable multilevel nonvolatile photonic random-access memory *Light* **12** 189

[42] Behera J K, Zhou X L, Tominaga J and Simpson R E 2017 Laser switching and characterisation of chalcogenides: systems, measurements, and applicability to photonics [Invited] *Opt. Mater. Express* **7** 3741–59

[43] Wang Y Z, Ning J, Lu L, Bosman M and Simpson R E 2021 A scheme for simulating multi-level phase change photonics materials *npj Comput. Mater.* **7** 183

[44] Sun X X, Lotnyk A, Ehrhardt M, Gerlach J W and Rauschenbach B 2017 Realization of multilevel states in phase-change thin films by fast laser pulse irradiation *Adv. Opt. Mater.* **5** 1700169

[45] Pérez-López D, López A, DasMahapatra P and Capmany J 2020 Multipurpose self-configuration of programmable photonic circuits *Nat. Commun.* **11** 6359

[46] Qu Y R, Li Q, Du K K, Cai L, Lu J and Qiu M 2017 Dynamic thermal emission control based on ultrathin plasmonic metamaterials including phase-changing material GST *Laser Photon. Rev.* **11** 1700091

[47] Clements W R, Humphreys P C, Metcalf B J, Kolthammer W S and Walmsley I A 2016 Optimal design for universal multiport interferometers *Optica* **3** 1460–5

Supplementary Materials for Pixelated non-volatile programmable photonic integrated circuits with 20-level intermediate states

State Key Laboratory of Intelligent Manufacturing Equipment and Technology, Huazhong University of Science and Technology, Wuhan 430074, People's Republic of China

* Corresponding authors: jinlongzhu03@hust.edu.cn, shyliu@hust.edu.cn

Supplementary 1: Ellipsometer of Sb_2S_3 samples

An ellipsometer (RC2, J.A. Woollam Co., Inc.) was used to measure the optical properties of aSbS and cSbS. The 10 nm-thick Sb_2S_3 films covered by 20 nm-thick SiO_2 films on silicon substrates were heated at different temperatures (240°C, 280°C, 320°C, 360°C). The Tauc-Lorentz oscillator model is used to fit the measurement results of aSbS and cSbS from 193 nm to 1 690 nm wavelengths. The parameters of the fitted Tauc-Lorentz model of aSbS and cSbS are shown in **Table S1** below.

Table S1. The parameters of Gen-Osc models of aSbS and cSbS.

aSbS		cSbS	
1: Type: Tauc-Lorentz	2: Type: Tauc-Lorentz	1: Type: Tauc-Lorentz	2: Type: Tauc-Lorentz
Amp1=167.201 4 ±1.231 38	Amp2=21.178 4 ±0.227 45	Amp1=157.792 8 ±1.871 09	Amp2=33.761 0 ±1.138 96
Br1=3.409 ±0.010 7	Br2=66.846 ±9 999.000 0	Br1=2.125 ±0.014 0	Br2=66.846 ±9 999.000 0
Eo1=3.412 ±0.004 864	Eo2=15.000 ±0.675 0	Eo1=3.094 ±0.007 989	Eo2=7.981 ±0.332 2
Eg1=2.040 ±0.002 380	Eg2=(Coupled)	Eg1=1.527 ±0.004 189	Eg2=(Coupled)
MSE=2.800		MSE=2.658	

Supplementary 2: Laser-writing multi-level intermediate Sb_2S_3 elements

The image of the experimental setup is shown in **Figure S1**. The diode laser (Thorlabs, L520P50) was used to realize the partial crystallization of Sb_2S_3. A 0.6 NA/50X objective lens (Nikon) was used in our system to focus the laser beam. The Sb_2S_3 sample was mounted on a three-axis stage (Thorlabs, MT3-Z8). The pulse sequence was generated by the arbitrary waveform function generator (RIGOL, DG2102). An optical power meter (Thorlabs, PM121D) was used to measure the power of the diode laser.

Due to the low optical absorption of aSbS, it is easy to cause local damage and ablation of Sb_2S_3 elements with a single high-power and long-duration laser pulse. Moreover, the intensity in the focused laser center is much higher than that in the laser edge due to the gaussian distribution of the intensity in the laser spot. Thus, Sb_2S_3 in the laser spot is easier to ablate. **Figure S2**(a) shows the local

damage to the 70-nm thick Sb_2S_3 elements induced by a single high-power laser. As a comparison, the local damage of the 26.8-nm thick Sb_2S_3 film is shown in **Figure S2**(b).
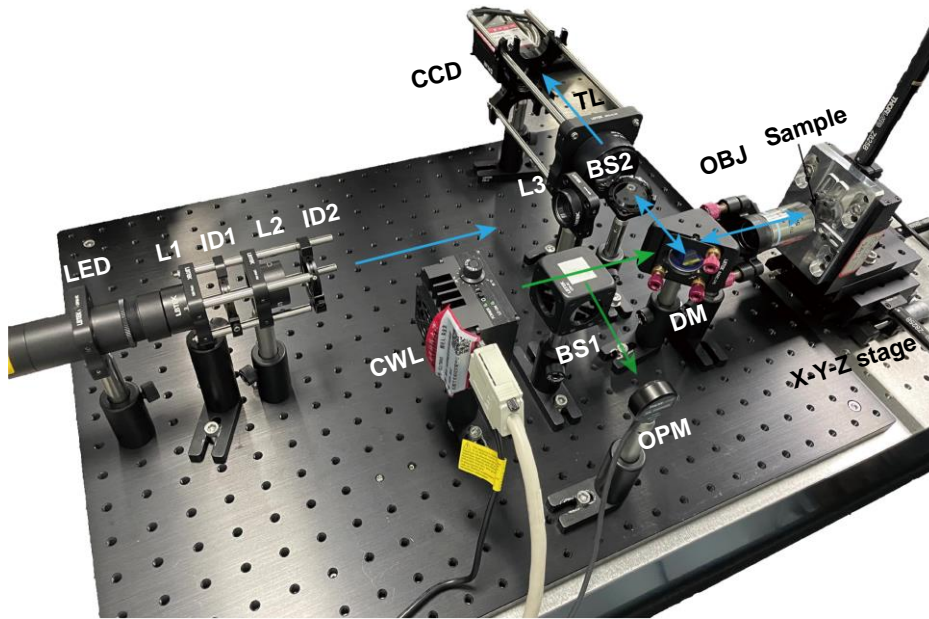

Figure S1. The experimental setup of the pulsed laser writing system. L, lens; ID, iris diaphragm; CWL: continuous wave lasers; BS, beam splitter; OPM, optical power meter; DM,dichroic mirror; OBJ, objective lens; TL, tube lens.
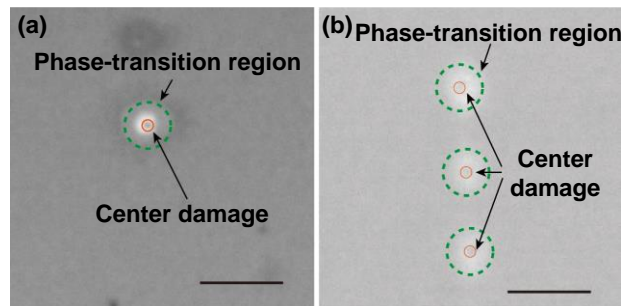

Figure S2. The center damage of the phase-transition elements of (a) a 70-nm thick Sb_2S_3 film and(b) a 26.83-nm thick Sb_2S_3 film.

In the laser-writing experiment, we leverage laser pulse sequences from 0 to 350 pulses to crystallize Sb_2S_3, and the step is 1 pulse. In order to guarantee the distinct reflectance difference (*ΔR*) of multi-level intermediate states, we set 10 pulses as the crystallization step to improve the stability of the degree of crystallization. The whole 20-level images of intermediate Sb_2S_3 pixels are shown in **Figure S3**. The *ΔR* of 20-level intermediate Sb_2S_3 pixels are detailed in **Table S2**. It is worth noting that more intermediate states of PCMs could be obtained with more accurate measurement technologies and devices in this way.
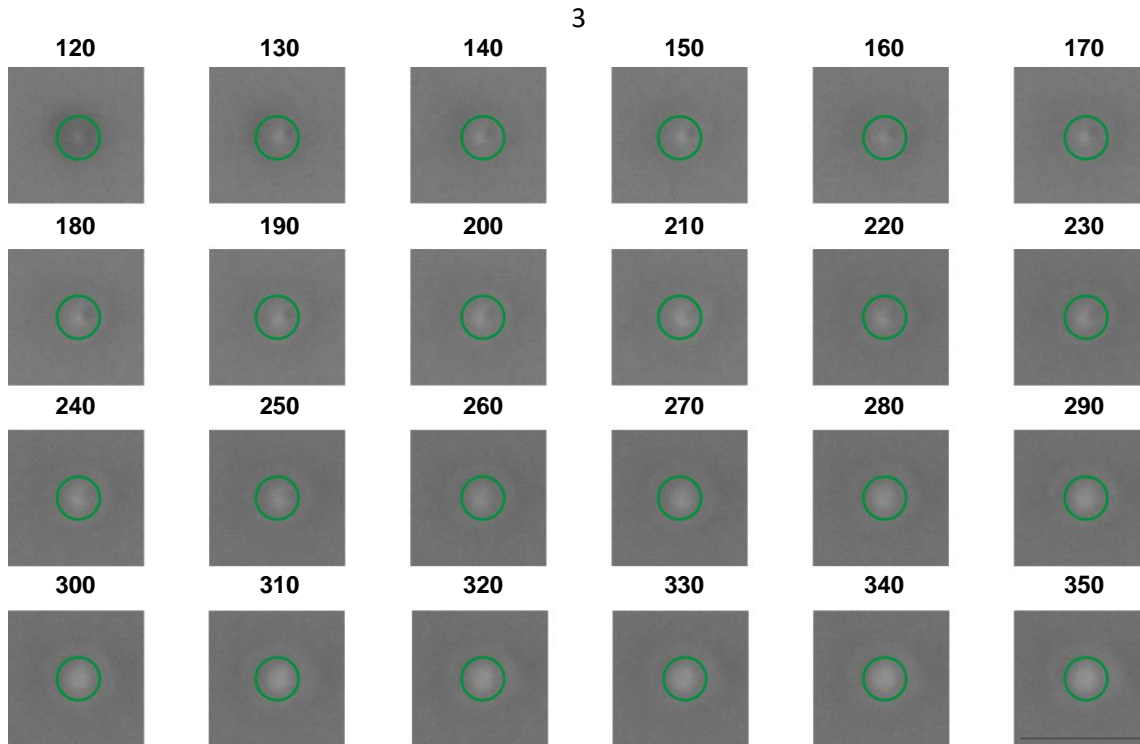
Figure S3. The whole 20-level intermediate Sb_2S_3 pixels images from 120 to 350 pulses. Scale bar: 5 μm.

Table S2. The reflectance difference (ΔR) of 20-level intermediate Sb_2S_3 pixels.

Pulse Number	ΔR
120	0.105
130	0.210
140	0.223
150	0.241
160	0.255
170	0.287
180	0.299
190	0.309
200	0.329
210	0.347
220	0.379
230	0.414
240	0.421
250	0.435
260	0.471
270	0.499
280	0.505
290	0.525
300	0.538
310	0.561
320	0.569

330	0.579
340	0.576
350	0.583

Supplementary 3: 5-level intermediate states of 10 nm-thick Sb₂S₃ pixels

All of the 5-level intermediate states of 10 nm-thick Sb_2S_3 pixels images are shown in **Figure S4**. The degree of crystallization could be determined by the reflectance based on the transfer matrix method (TMM). The effective permittivity (ε_{eff}) and the refractive index of intermediate Sb_2S_3 pixels can be calculated according to the Lorentz-Lorenz relation.

$$\frac{\varepsilon_{eff}(\lambda)-1}{\varepsilon_{eff}(\lambda)+2} = m \times \frac{\varepsilon_c(\lambda)-1}{\varepsilon_c(\lambda)+2} + (1-m) \times \frac{\varepsilon_a(\lambda)-1}{\varepsilon_a(\lambda)+2}, \tag{1}$$

where m is the crystalline fraction of Sb_2S_3, $\varepsilon_c(\lambda)$, $\varepsilon_a(\lambda)$ are the permittivity of the cSbS and aSbS. The optical properties of 5-level intermediate states at 785 nm wavelength are detailed in **Table S3**.
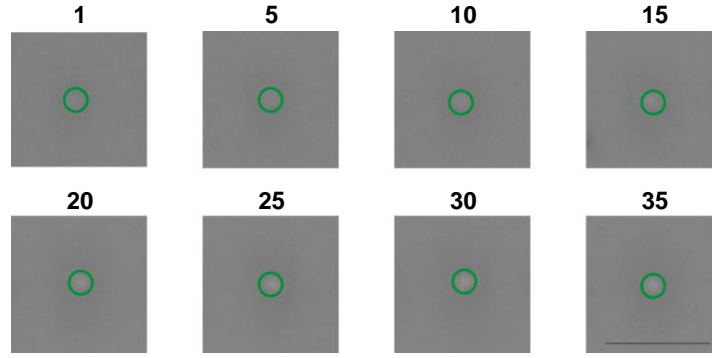

Figure S4. 5-level intermediate Sb_2S_3 pixels images from 1 to 35 pulses. Scale bar: 5 μm.

Table S3. The optical properties of 5-level intermediate states of 10 nm-thick Sb_2S_3 pixels.

Level	Crystalline Fraction	n_{eff}	k_{eff}
1	0	2.75	0
2	0.35	3.042	0.000 777
3	0.66	3.355	0.001 82
4	0.82	3.561	0.002 635
5	0.88	3.643	0.002 985
6	1	3.819	0.003 8

Supplementary 4: Simulation of pixelated programmable silicon nitride photonic circuits based on Sb₂S₃ matrix

The film of Sb_2S_3 is deposited on the waveguide to shift optical phase, and L_π is the length to realize π phase. The calculation formula of the Sb_2S_3 length L_π is given by

$$L_\pi = \frac{\lambda}{2 \times (N_{ceff} - N_{aeff})},$$ (2)

where N_{ceff} and N_{aeff} are effective refractive indexes of waveguide covered by cSbS and aSbS, respectively. The complete 30-level phase values are given in **Table S4**.

The mode overlaps between the bare waveguide and the waveguide covered with Sb_2S_3 film also induces insertion loss except for the absorption from Sb_2S_3 film. The field overlaps between the mode in the bare waveguide and that covered with different thicknesses aSbS is calculated, as shown in **Figure S5**(a).

Sb_2S_3 is used to achieve the complete π phase modulation in the balanced MZI, as shown in **Figure S5**(b). If we consider the 2×2 MMI or directional coupler for the perfect beam splitter (50:50 ratio), the transmission of the MZI is given by

$$\begin{pmatrix} E_{o1} \\ E_{o2} \end{pmatrix} = \frac{1}{2} \begin{pmatrix} 1 & i \\ i & 1 \end{pmatrix} \begin{pmatrix} A_1\exp(i\theta_1) & 0 \\ 0 & A_2\exp(i\theta_2) \end{pmatrix} \begin{pmatrix} 1 & i \\ i & 1 \end{pmatrix} \begin{pmatrix} E_{i1} \\ E_{i2} \end{pmatrix},$$ (3)

where A_1 and A_2 are the optical losses caused by Sb_2S_3 in each waveguide arm, and θ_1 and θ_2 are the phase shifts in each waveguide arm. Here, we only change θ_1 and A_1 to obtain 30-level E_{o1} and E_{o2}. The Sb_2S_3 in the lower waveguide (θ_2 and A_2) is used to compensate for insertion loss.

Table S4. The 30-level phase values of the Sb_2S_3-based phase shifter.

Level	Phase(rad)
1	0.117
2	0.264
3	0.375
4	0.422
5	0.532
6	0.649
7	0.796
8	0.906
9	0.954
10	1.064
11	1.181
12	1.327
13	1.438
14	1.486
15	1.596
16	1.712
17	1.859

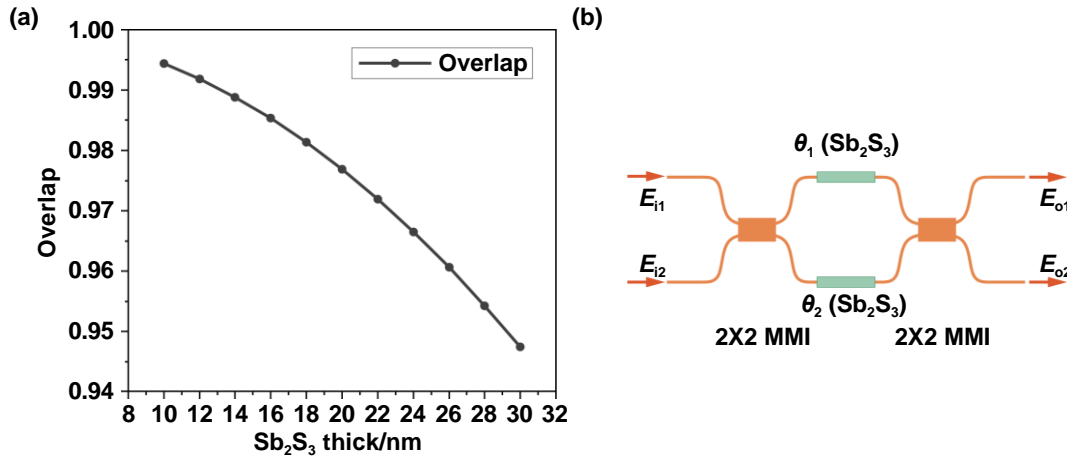|	
18	1.970
19	2.018
20	2.127
21	2.244
22	2.391
23	2.502
24	2.550
25	2.659
26	2.776
27	2.923
28	3.034
29	3.082
30	3.191

Figure S5. Simulation results of pixelated programmable silicon nitride photonic circuits. (a) Mode overlaps between the bare waveguide and waveguide covered with different thickness aSbS. (b) The schematic diagram of the programmable balanced MZI based on Sb_2S_3.

Supplementary 5: Programmable MMI based on Sb_2S_3 matrix

The programmable Sb_2S_3-matrix-based MMI is iteratively optimized based on multiple-value search algorithm. A random pattern is provided as the initial guess. A state of one Sb_2S_3 pixel is switched, and the FOM is simulated and calculated in one simulation. The state of the pixel is retained if the FOM is improved, otherwise, the pixel is brought back to its previous state. All 68 pixels (4×17) with six states are simulated in one iteration. When the FOM stops from improvement after several iterations, we can ensure that the best results are obtained. The multiple-value search algorithm is shown in **Figure S6**. The FOM is defined as:

$$FOM = -T_{low} \tag{4}$$

where T_{low} is the transmissions of the lower waveguide. The simulation is performed by the 3D eigenmode expansion method (Lumerical MODE).
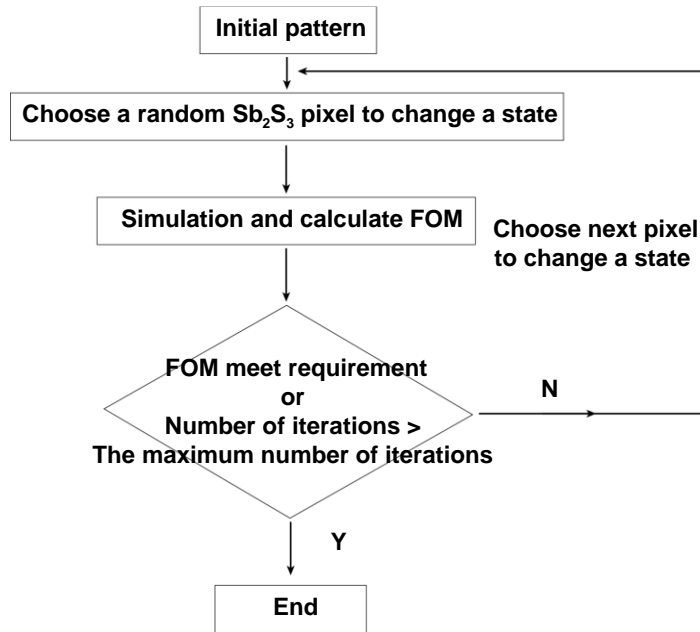

Figure S6. The multiple-value search algorithm.

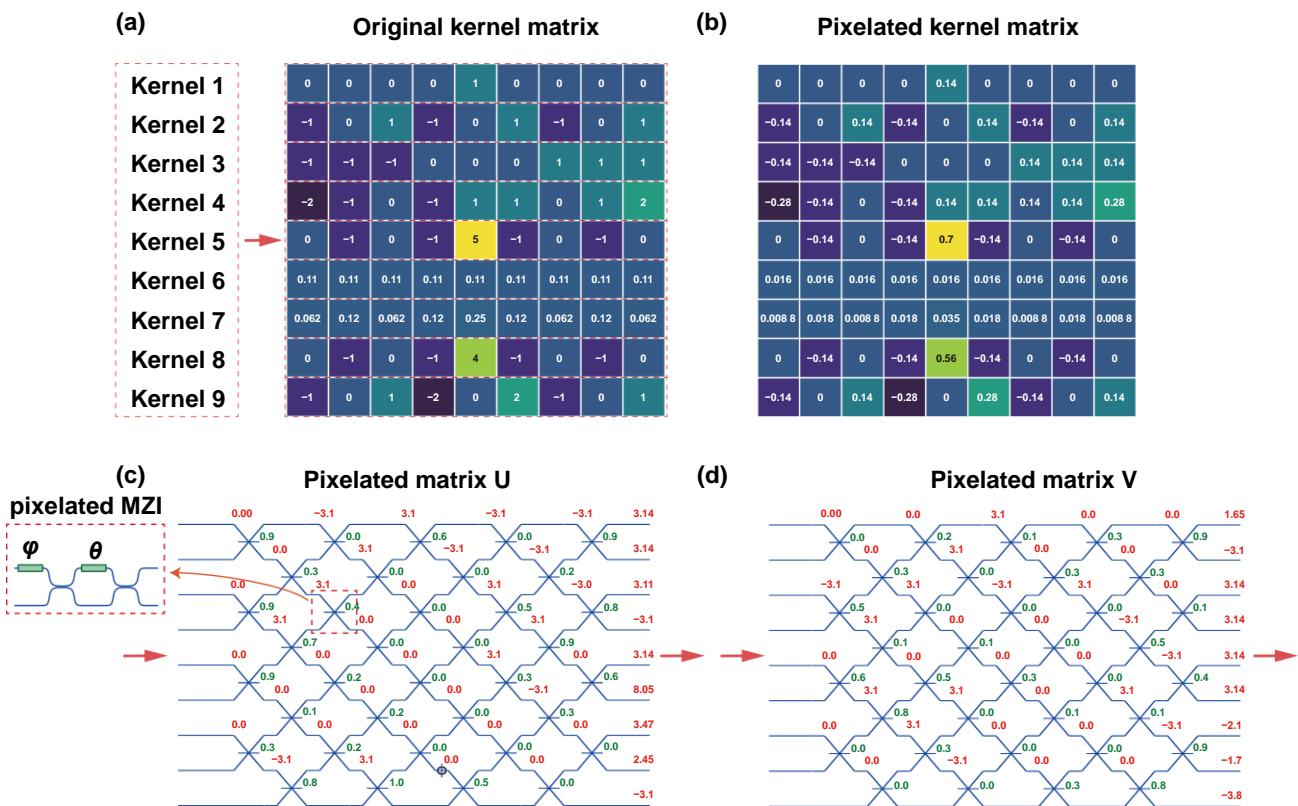# Supplementary 6: Pixelated programmable MZI-based photonic linear processor

Figure S7. Pixelated programmable MZI-based photonic linear processor. (a) The original 9×9 kernel matrix. (b) The normalized pixelated kernel matrix. (c) The phase shift values of pixelated matrix *U*. (d) The phase shift values of pixelated matrix *V*.

Supplementary 7: Single-layer continuous varifocal metalens based on multi-level Sb₂S₃

In order to showcase the potential applications of multi-level Sb₂S₃ in programmable metasurfaces, we simulated a single-layer continuous varifocal metalens at 1 550 nm wavelength based on the principle of propagation-phase-based metasurfaces, which are not affected by the polarization state of the incident light, as shown in **Figure S8**. The phase delay equation in conventional propagation phase design can be expressed as $\varphi = \dfrac{2\pi}{\lambda} n_{eff} H$, where n_{eff} is the effective refractive index of the nanopillar, and *H* is the height of the nanopillar. The n_{eff} of nanopillar can be adjusted by changing the diameter of the nanopillar. Unlike the conventional propagation-phase-based metalens, the effective refractive index and phase delay of each Sb₂S₃ cell can be modified by switching the level of intermediate states and maintaining a fixed periodic structure. By adjusting the intermediate states of Sb₂S₃ cells, the focal length of the metalens can be manipulated. An isolated Sb₂S₃ cell is shown in **Figure S8**(a). The height *h* of a Sb₂S₃ nanopillar is 1.9 μm to ensure a complete 2π phase delay, and a 200 nm-thick SiO₂ layer is deposited on the Sb₂S₃ nanopillars. The period *p* and the width d_1 of Sb₂S₃ nanopillar are 0.7 μm and 0.35 μm, respectively. In order to avoid mutual interference during laser writing, period *p* and width d_1 must satisfy the following inequalities: $2p - d_1 > d_{laser}$. The refractive indices of aSbS and cSbS are 2.61 and 3.45, respectively, based on the measured data at 1 550 nm wavelength. The finite difference time domain (FDTD) solver is used to simulate the transmission and the phase delays of isolated Sb₂S₃ cell, and the periodic boundary conditions are used. These optimized design parameters (p, h, d_1) of Sb₂S₃ nanopillars can achieve a complete 2π phase delay and high transmission, as shown in **Figure S8**(b).

The ideal phase profile of the metalens is given by:

$$\varphi(r_i) = -\frac{2\pi}{\lambda}(\sqrt{r_i^2 + f^2} - f), \tag{5}$$

where r_i is the radial distance from the center of the metalens, f is the focal length, and λ is the wavelength of incident light (1 550 nm). The desired phase delays at various radial positions (r_i) are discretized into 20-level phase values, achieved by using different intermediate states of Sb₂S₃. In order to demonstrate the varifocal metalens, we perform simulations using a FDTD solver with three different focal lengths (100 μm, 200 μm and 300 μm). The diameter *D* of the metalens is 400 μm.

According to the equation: $NA = \sin[\tan^{-1}(D/2f)]$, the numerical apertures (NAs) of the varifocal metalens, which correspond to the three focal lengths, are 0.81, 0.57 and 0.42, respectively. The far field of the metalens is calculated using the near-to-far-field transformation. **Figure S8**(c) illustrates the cross-section of the normalized intensity of the three focal spots along the *x* axis. **Figure S8**(d) shows the simulated intensity distribution of the three focal spots in the *x-y* plane. This simulation demonstrates the feasibility of a single-layer varifocal metalens based on the multi-level intermediate states of Sb_2S_3.
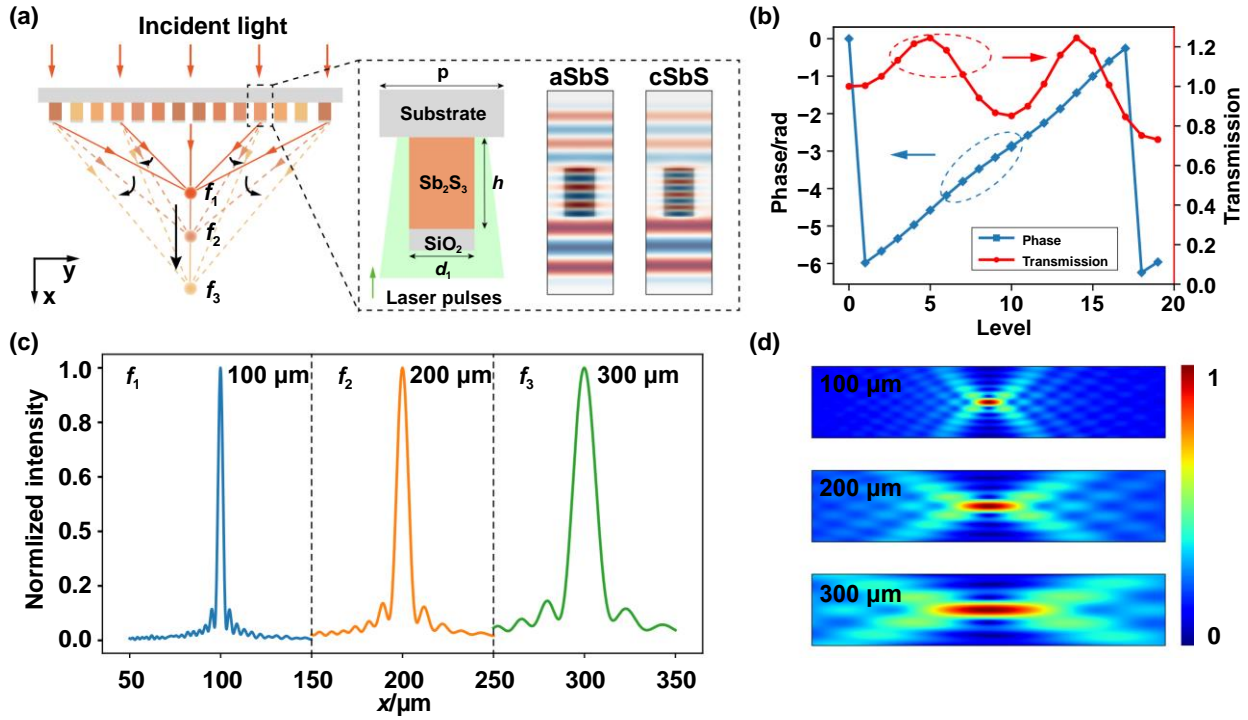

Figure S8. Single-layer continuous varifocal metalens based on multi-level Sb_2S_3. (a) The schematic diagram of the single-layer varifocal metalens based on multi-level Sb_2S_3 cells. The inset denotes the structure of an isolated cell alongside its electric field distribution at aSbS and cSbS states, respectively. (b) The phase delays and transmission of the 20-level intermediate states of Sb_2S_3. (c) The simulated normalized intensity profiles along the optical axis of three different focal spots. (d) The simulated electrical field in the *x-y* plane of different focal spots (100 μm, 200 μm and 300 μm).